Monthly Notices
of the
ROYAL ASTRONOMICAL SOCIETY

Mon. Not. R. Astron. Soc. **407,** 71–82 (2010) doi:10.1111/j.1365-2966.2010.16916.x

Photometric characterization of exoplanets using angular and spectral differential imaging

A. Vigan,[1⋆] C. Moutou,[1] M. Langlois,[2] F. Allard,[3] A. Boccaletti,[4] M. Carbillet,[5] D. Mouillet[6] and I. Smith[5]

[1]*LAM, UMR 6110, CNRS, Université de Provence, 38 rue Frédéric Joliot-Curie, 13388 Marseille Cedex 13, France*
[2]*CRAL, UMR 5574, CNRS, Université Lyon 1, 9 avenue Charles André, 69561 Saint Genis Laval Cedex, France*
[3]*CRAL, UMR 5574, CNRS, Université Lyon 1, ENS Lyon, 46 allée d'Italie, 69364 Lyon Cedex 07, France*
[4]*LESIA, UMR 8109, Observatoire de Paris, CNRS, Université Paris-Diderot, 5 place Jules Janssen, 92195 Meudon Cedex, France*
[5]*Laboratoire Fizeau, UMR 6525, CNRS, Université de Nice Sophia Antipolis, Observatoire de la Côte d'Azur, Parc Valrose, 06108 Nice Cedex 2, France*
[6]*LAOG, UMR 5571, CNRS, Université Joseph-Fourier, BP 53, 38041 Grenoble Cedex 9, France*

Accepted 2010 April 23. Received 2010 April 21; in original form 2010 March 23

ABSTRACT

In recent years, there has been intensive research into the direct detection of exoplanets. Data obtained in the future with high-contrast imaging instruments, optimized for the direct detection of giant planets, may be strongly limited by speckle noise. Specific observing strategies and data analysis methods, such as angular and spectral differential imaging, are required to attenuate the noise level and possibly to detect the flux of faint planets. Even though these methods are very efficient at suppressing the speckles, the photometry of faint planets is dominated by the speckle residuals. The determination of the effective temperature and surface gravity of the detected planets from photometric measurements in different bands is then limited by the photometric error on the planet flux. In this paper, we investigate this photometric error and the consequences on the determination of the physical parameters of the detected planets. We perform detailed end-to-end simulation with the CAOS-based software package for spectro-polarimetric high-contrast exoplanet research (SPHERE) to obtain realistic data representing typical observing sequences in the Y, J, H and K_s bands with a high-contrast imager. The simulated data are used to measure the photometric accuracy as a function of contrast for planets detected with angular and spectral+angular differential methods. We apply this empirical accuracy to study the characterization capabilities of a high-contrast differential imager. We show that the expected photometric performances will allow the detection and characterization of exoplanets down to a Jupiter mass at angular separations of 1.0 and 0.2 arcsec, respectively, around high-mass and low-mass stars with two observations in different filter pairs. We also show that the determination of the physical parameters of the planets from photometric measurements in different filter pairs is essentially limited by the error on the determination of the surface gravity.

Key words: methods: data analysis – techniques: high angular resolution – techniques: photometric – infrared: planetary systems.

1 INTRODUCTION

Since the detection of the first exoplanet orbiting a main-sequence star, 51 Peg, a large population of these objects has been discovered. These cover a wide range of masses and orbital periods, and they have been found mostly using indirect methods, such as radial-velocity measurements and transits (see, for example, Santos 2008 for a review). Although mainly sensitive to planets with periods of less than 10 yr, radial-velocity surveys have found stars that start to show long-term trends, indicating possible low-mass companions orbiting at large orbital separations (Wittenmyer, Endl & Cochran 2007). The wide use of adaptive optics (AO) systems and coronagraphy in large-telescope instrumentation for high-contrast imaging has allowed us to start probing the vicinity of nearby stars for low-mass companions at large orbital separations. Over the last decade, a handful of objects close to the planetary mass regime have been imaged with existing instruments, such as 2M 1207 b (Chauvin et al.

⋆E-mail: arthur.vigan@oamp.fr

2005a), DH Tau B (Itoh et al. 2005), GQ Lup b (Neuhäuser et al. 2005), AB Pictoris b (Chauvin et al. 2005b), CHXR 73 B (Luhman et al. 2006) and, more recently, Fomalhaut b (Kalas et al. 2008), 1RXS J1609 b (Lafrenière, Jayawardhana & van Kerkwijk 2008), β Pictoris b (Lagrange et al. 2009) and the triple system around HR 8799 (Marois et al. 2008b). However, the large uncertainty on the mass of these objects may place some of them in the substellar rather than the planetary mass regime.

The next generation of planet-finding instruments currently being built will combine (i) extreme AO systems with a large number of actuators (Angel 1994; Stahl & Sandler 1995; Langlois 2001) to reach very high corrections in the near-infrared (Fusco et al. 2006; Aller-Carpentier et al. 2008) and (ii) high-efficiency coronagraphs, such as the apodized pupil Lyot coronagraph (Soummer 2005 and references therein) or the achromatic four-quadrant phase mask (Rouan et al. 2000; Mawet et al. 2006) to obtain optimal star extinction. The Gemini planet imager (GPI) for Gemini South (Macintosh et al. 2006) and the spectro-polarimetric high-contrast exoplanet research (SPHERE) for the European Southern Observatory (ESO) Very Large Telescope (VLT) (Beuzit et al. 2006) are the two leading instruments of that category. These will both start operation in 2011, along with the high-contrast coronagraphic imager for adaptive optics (HiCIAO) for *Subaru* (Hodapp et al. 2008). These will aim to detect exoplanets down to the Jupiter mass (M_{Jup}) around nearby young stars by reaching contrast values of 15–17.5 mag (10^{-6}–10^{-7}) at angular separations of $\sim$0.1 arcsec. Both GPI and SPHERE will incorporate diffraction-limited integral field spectrographs (IFSs) in the near-infrared, allowing us to obtain images simultaneously at several wavelengths. SPHERE will also incorporate a differential imager, called the infrared dual imaging spectrograph (IRDIS; Dohlen et al. 2008a), which will provide simultaneous images at two close wavelengths in any one of its five different filter pairs over the Y to K_s bands.

These instruments will allow us to use different observing strategies, such as spectral differential imaging (SDI; Racine et al. 1999) or angular differential imaging (ADI; Marois et al. 2006) to obtain data that will be analysed using advanced methods, such as spectral deconvolution (Sparks & Ford 2002) or locally optimized combination of images (LOCI; Lafrenière et al. 2007) for the IRDIS data. Specific methods of signal extraction have also been developed within the SPHERE consortium (Mugnier et al. 2008; Smith, Ferrari & Carbillet 2009) to be used in the data reduction pipeline of IRDIS. Data analysis methods are of extreme importance when it comes to the detection of faint objects in coronagraphic images dominated by speckles. In particular, the precise estimation of the object flux after applying these methods is critical for the calibration of the model atmospheres of planetary-mass objects (Ackerman & Marley 2001; Allard et al. 2001, 2003, 2007, and in preparation; Tsuji 2005; Burrows, Sudarsky & Hubeny 2006) based on the effective temperature (T_{eff}) and the surface gravity ($\log g$), and the corresponding evolutionary models (Burrows et al. 1997; Chabrier et al. 2000; Baraffe et al. 2003; Fortney et al. 2005). The only currently available method for mass estimation, when no dynamical mass estimations are known for the object, consists of incorporating photometric measurements and their error assessment into these physical models. Although spectroscopy is the method of choice for characterization, it may not be possible to obtain high-quality spectra of extremely faint sources (Vigan et al. 2008; Janson et al. 2010).

In this paper, we investigate the photometric limitations in high-contrast data obtained at different wavelengths with a dual-band imager such as IRDIS, and we study how this translates in terms of characterization of planetary-mass objects. After recalling in Section 2 the origin of speckle noise, which is the fundamental limitation in high-contrast imaging, and the methods to overcome it, we present in Section 3 the end-to-end simulations of IRDIS, which were performed to obtain a realistic observing sequence. In Section 4 we briefly describe the detection limits obtained with ADI and SDI+ADI data analysis methods, before studying the performances in terms of photometric accuracy. Finally, in Section 5 we advocate a filter pair procedure for IRDIS and we present an analysis of the characterizations that will be possible using aperture photometry.

2 LIMITATIONS IN HIGH-CONTRAST IMAGING

To detect very faint planetary objects, it is necessary to obtain diffraction-limited images with high-order AO systems in order to overcome the large contrast ratio between the star and the planet with coronagraphy. In high-Strehl ratio coronagraphic images, the factor that limits the accessible dynamical range is the speckle noise (Soummer et al. 2007) induced by atmospheric phase residuals and instrumental quasi-static aberrations not corrected by the AO system. The quasi-static speckles are caused by the instrumental aberrations that slowly change during a long exposure. Telescope orientation, temperature variations or rotating optical elements cause small mechanical variations in the optical elements, which make the speckle pattern evolve. Long time exposures are typically decomposed in a series of short exposure images of a few seconds, during which the atmospheric residuals are averaged out, forming a smooth halo over which the quasi-static speckles are superimposed, because their coherence time is much longer than the atmospheric residuals (Langlois et al. 1998; Macintosh et al. 2005; Hinkley et al. 2007). To optimize AO performances and speckle rejection, observations can be performed in pupil-stabilized mode, leading to a very high stability of the star's point spread function (PSF) and a slow rotation of the field of view during the observations, at a rate that depends on the star's position in the sky.

The speckle noise can be reduced by subtracting a reference PSF from each science frame in order to remove the star halo and speckles, and possibly reveal a faint planetary object. This reference PSF can be obtained by observing a reference star taken in the same observing conditions (parallactic angle and atmospheric conditions, if possible) as the original target to reproduce a similar pattern of quasi-static speckles. This is a very time-consuming task because the time spent on the reference star is equal to that spent on the target in order to precisely match both PSFs, and the aberrations between the two stars cannot be exactly reproduced. The reference can also be built from the science frames by using either spectral or angular information.

The SDI method was first proposed by Racine et al. (1999) for the detection of faint companions. It has been extensively studied (Marois et al. 2000), and subsequently tested on the sky with TRIDENT on the Canada–France–Hawaii Telescope (CFHT; Marois et al. 2005) and with NaCo on the VLT (Lenzen et al. 2004). The technique relies on the fact that planetary objects have large intrinsic molecular features in their spectrum, while the host star has a relatively flat spectrum. By taking simultaneously two images of a system at two close wavelengths located around one of these sharp features and subtracting them, the star contribution can be partially eliminated, and the planet signal revealed. SDI is most effective when used for detecting cool companions that show deep molecular absorption bands caused by H_2O, CH_4 and NH_3 at low T_{eff}, according to state-of-the-art atmosphere models of planetary-mass

objects. With carefully selected filter pairs, a contrast of several magnitudes on the planet flux between the two filters can be obtained. However, the presence of the molecular features expected for the detection of cool planetary companions should not be taken for granted, as recent atmosphere models (Fortney et al. 2008), as well as observations of 2M1207b (Mohanty et al. 2007; Patience et al. 2010) and the HR 8799 planets (Marois et al. 2008b; Metchev, Marois & Zuckerman 2009; Janson et al. 2010), seem to show that non-equilibrium CO/CH_4 chemistry could play an important role in young low-surface-gravity objects. In particular, the CH_4 band head near 1.6 μm could appear at much lower $T_{\rm eff}$ than predicted by current atmosphere models. The SDI method is straightforward to implement: the images taken at λ_1 need to be spatially rescaled to account for the spectral dependence of the PSF and subtracted from the images at λ_0, with a possible amplitude correction factor to minimize the residual speckle noise. The main advantage of SDI is to significantly reduce the seeing halo, but it is intrinsically limited by speckle chromaticity and differential aberrations when going through two separate optical paths.

The ADI method proposed by Marois et al. (2006) requires observations made in pupil-stabilized mode. It uses the field rotation to build an optimized reference PSF that contains very little signal from the planet. For each image I_i, a reference PSF is calculated using images taken before and images taken after, and for which a field rotation of at least 1.5 λ/D has occurred in between. These images are then combined to eliminate the planet signal and produce a reference PSF that is subtracted from the image I_i. These operations are performed for all images in annuli of increasing radius. A thorough description of the complete procedure can be found in section 5.2 of Marois et al. (2006). This technique is essentially limited by the temporal evolution of the speckles, which cannot be controlled. The global efficiency of the ADI method is controlled by the rotation rate of the field of view, which depends on the star declination, and by the angular separation, which constrains the actual motion on the detector. At the latitude of the ESO Paranal observatory ($-24^\circ 3' 38''$) and for a star at declination $\delta = -45^\circ$, the field rotation varies between 0.006 deg s^{-1} at an hour angle of ±2 h and 0.011 deg s^{-1} at an hour angle of 0 h. This defines a strong constraint on the telescope time necessary to calibrate the speckles.

Finally, the SDI and ADI methods can be efficiently combined to further reduce the speckle noise. SDI is first performed on short-exposure images acquired simultaneously to remove the fast varying atmospheric residuals that have not been averaged out. ADI is subsequently applied on this set of data to combine the images with different angular positions of the field of view.

3 END-TO-END SIMULATIONS

A complete end-to-end model of SPHERE has been developed to test the instrument performances and different data analysis methods. This model is a diffractive code written in interactive data language (IDL) based on the code for adaptive optics system (CAOS) problem-solving environment (Carbillet et al. 2004) with a specific package developed for the SPHERE project (Carbillet et al. 2008).

Realistic data cubes have been simulated to represent typical 4-h exposure with IRDIS and an apodized Lyot coronagraph at different wavelengths where the star goes from −2 to +2 h angles. Every data cube is composed of 144 images, each representing a cumulative 100 s exposure, and several parameters are modified in the course of the simulation to take into account the variations of optical aberrations on a long time-scale. The seeing and wind speed have been varied on ranges typical for the ESO Paranal observatory, 0.85 ± 0.15 arcsec and 14.2 ± 4.6 m s^{-1}, respectively. For each individual image, the AO-corrected atmosphere was simulated by a set of 100 decorrelated phase screens. The typical millisecond time-scale of the uncorrected atmospheric residuals is not considered here. We assume that on a 100-s time-scale, these residuals are averaged out and produce a smooth halo; only the correlated residuals with time-scales longer than a few hundred seconds will remain. From the instrumental point of view, variations of the beam shift as well as rotation of the entrance window, atmospheric dispersion corrector (ADC) and derotator have been translated into wavefront error. Chromatic shifts associated with the ADC have been calculated from its optical design. Slow achromatic drifts, such as defocus and tilt, associated with temperature changes have been added. Finally, differential aberrations between the two filters in the differential imager have been taken into account. Considering the prototypes of IRDIS DBI filters (Dohlen et al. 2008b), 7.55-nm rms of differential aberrations have been introduced.

In these end-to-end simulations, the Fresnel propagation of the wavefront is not considered. However, the overall impact of Fresnel propagation has been evaluated in separate simulations (not detailed here) where pre-coronagraphic and post-coronagraphic propagation effects have been simulated. The main result is that while the region beyond AO cut-off (0.8 arcsec in the *H* band) is mostly dominated by the pre-coronagraphic propagation effects, resulting in a loss of up to a factor of 2 in contrast, the inner region is affected by a mix of both effects, resulting in a loss of at most 1.5.

Four complete data cubes have been simulated, corresponding to the filter pairs Y2Y3, J2J3, H2H3 and K1K2 of IRDIS (Table 1). The output of the diffractive code is a series of normalized coronagraphic and non-coronagraphic images of the star at the two wavelengths of the considered filter pair. A second code was used to create data cubes representing realistic planetary systems. For each star, three series of planets separated by 120° have been simulated at 0.2, 0.5, 1.0, 1.5 and 2.0 arcsec, taking into account the slow field rotation, which is a function of the star elevation. The star was chosen at a declination of −45° and an hour angle of −2 h at the beginning of the simulated observation, representing a total field rotation of ∼120°.

To calculate realistic photometry, we used standard Kurucz models (Kurucz 1979; Castelli & Kurucz 2003) for stars with spectral types regularly distributed from F0 to M0 at a distance of 10 pc ($V = 2.7$–8.8). For the planets, we constituted a library of ∼220 synthetic spectra including the AMES–DUSTY models of Allard et al. (2001), the BT–SETTL models of Allard et al. (2007), the AMES–COND models of Allard et al. (2003) and the models of Burrows et al. (2006), with effective temperature ranging from $T_{\rm eff} = 350$ K to $T_{\rm eff} = 2500$ K, and surface gravity ranging from $\log g = 2.5$ to $\log g = 6.0$. The steps in the grids of models are of 100 K in $T_{\rm eff}$ and 0.5 in $\log g$. We assume these models are complementary, and

Table 1. List of IRDIS filter pairs.

Pair name	Filter 0		Filter 1	
	λ_0 (μm)	R_0	λ_1 (μm)	R_1
Y2Y3	1.020	20	1.073	20
J2J3	1.190	25	1.270	25
H2H3	1.587	30	1.667	30
H3H4	1.667	30	1.731	30
K1K2	2.100	20	2.244	20

Table 2. Atmosphere models included in our library.

Model	$T_{\rm eff}$ (K)	$\log g$ (dex)
AMES–COND[a]	350–1300	2.5–6.0
BT–SETTL[b]	1100–2300	4.5–5.5
AMES–DUSTY[c]	1700–2500	2.5–6.0
BSH[d]	700–2000	4.5–5.5

[a]Allard et al. (2003).
[b]Allard et al. (2007).
[c]Allard et al. (2001).
[d]Burrows et al. (2006).

Table 2 gives a list of the models with the $T_{\rm eff}$ and $\log g$ ranges over which they are considered. For each filter pair, we generated 66 data cubes with a different combination of star and planet models to cover contrast values from 5 to 16.5 mag ($\sim 2 \times 10^{-7}$ to $\sim 10^{-2}$).

In each data cube, the sky contribution has been added to match typical values for the ESO Paranal observatory. Thermal background from the instrument was also included: the value is low in the I, J and H bands (<2 photon s^{-1} pixel^{-1}), while it becomes significant in the K band (60–220 photon s^{-1} pixel^{-1}). The code also accounts for the global throughput of the instrument and the atmospheric transmission, but does not consider OH line variability. Finally, a realistic amount of noise for the IRDIS detector was included in the images: photon noise, flat-field noise (0.1 per cent) and readout noise (10 e$^-$/read).

The final output of the photometric code represents a 4-h observation with IRDIS after standard cosmetic correction and calibrations (dark, sky background and thermal background subtraction, flat-field division, bad pixel correction). Because of the large number of parameters taken into account and the important computing time required for the simulation, only one data set representing a standard case has been produced. This means that all generated data cubes present the same speckle pattern, and only differ by photometric and noise values.

ADI and SDI+ADI data analysis methods were then applied on all our simulated data cubes to attenuate the speckle noise. The ADI data analysis was implemented in IDL following the algorithm described by Marois et al. (2006): frames separated by 2.0 λ/D were selected and combined in five annuli covering our simulated planets to produce two final images for data taken at λ_0 and λ_1. The SDI data analysis was implemented in IDL using a custom routine for the precise spatial rescaling (L. Mugnier, private communication) based on zero-padding in both real and Fourier spaces. ADI was then applied on the subtraction of data taken at λ_0 and λ_1 to produce the final SDI+ADI image.

4 PHOTOMETRIC ACCURACY

4.1 Noise level with ADI and SDI+ADI

The 1σ noise levels were evaluated from the data products of the ADI and SDI+ADI data analysis methods by measuring the standard deviation of the residual speckle noise in annuli of increasing radius, normalized to the maximum of the PSF without coronagraph. It is known from Goodman (1968), Aime & Soummer (2004), Fitzgerald & Graham (2006) and Smith et al. (2009) that the speckle noise statistics in AO-corrected images with and without coronagraph is not Gaussian. However, Marois et al. (2008a) have shown that residual noise after applying ADI on $\sim$20 or more images is quasi-Gaussian. ADI was applied on our data cubes with more than 20 images in every case, so we consider the residual noise as Gaussian and we use the standard 5σ level for detection limits

Fig. 1 shows the 1σ noise level for the H2H3 filter pair in two different regimes: a high-flux case corresponding to a high-mass star (F0 star at 10 pc, $V = 2.7$) and a low-flux case corresponding to a lower-mass star (M0 star at 10 pc, $V = 8.8$). The ADI noise level in filter H3 is not shown because it is at the same level as in filter H2. In high flux, the speckle noise attenuation is almost constant from 0.1 arcsec (inner-working angle of the coronagraph) to 2.5 arcsec, both with ADI and SDI+ADI, allowing us to reach a contrast of $\sim$16 mag at 0.2 arcsec and more than 20 mag at 2.5 arcsec. In low flux, the level of the background noise (sky and instrumental thermal emission, readout noise) becomes limiting, and the attenuation reaches an almost constant level in SDI+ADI at 1.5 arcsec. The

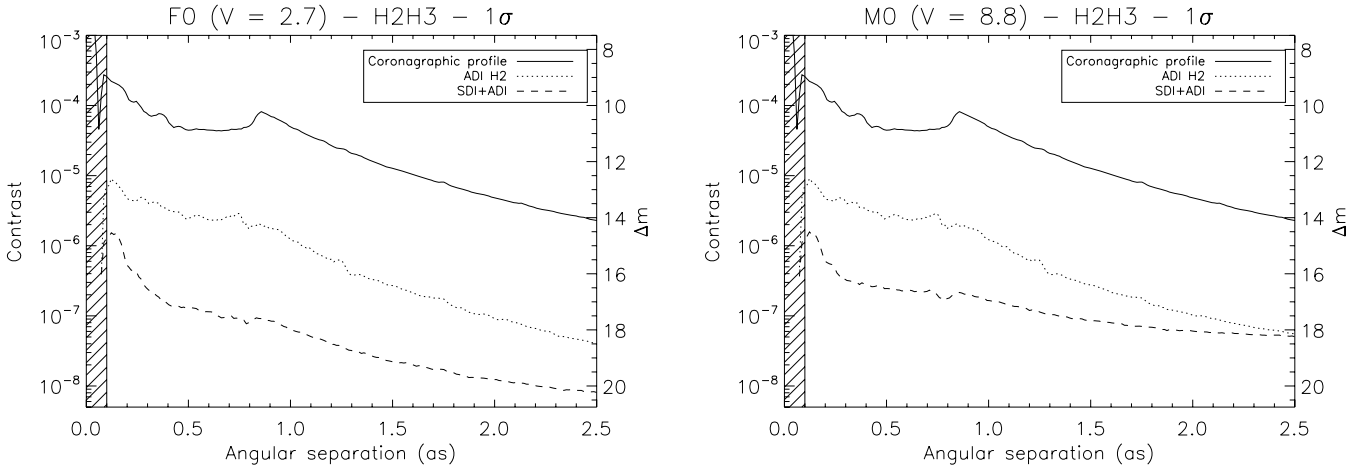

Figure 1. 1σ noise levels after applying ADI and SDI+ADI data analysis methods in the H band for high-mass (left, F0 at 10 pc, $V = 2.7$) and low-mass (right, M0 at 10 pc, $V = 8.8$) stars during a 4-h exposure time. The hatched area below 0.1 arcsec is covered by the opaque coronagraphic mask. The coronagraphic profile is calculated by the average of the coronagraphic image in annuli of increasing radius, and the different noise levels by the standard deviation of the residuals in the same annuli. All curves are normalized to the maximum of the PSF without coronagraph.

noise levels are similar in the Y, J and H bands, but in the K band, where the thermal emission is 10–15 times higher than in the J or H bands, the accessible contrast in the low-flux regime is limited at 15.5 mag.

If we compare these 1σ noise levels to those derived for the IRDIS long slit spectroscopy (LSS) mode (Vigan et al. 2008), we see that they are comparable between ADI and LSS. However, SDI+ADI clearly brings an improvement of 2–3 mag compared to LSS, justifying the need to quantify characterization capabilities in DBI mode for planets that are not detectable with LSS.

4.2 Planet flux estimation

We have estimated the signal of all planets detected at more than 5σ with aperture photometry in a 2.44 λ/D radius aperture. The aperture is calculated to take into account the effect of using a round aperture on square pixels. The measured signal has been converted to a flux in phot s^{-1} m^{-2} with the formula:

$$f_i = \frac{S_i}{E_e S_{Tel} T_r t_i}. \quad (1)$$

Here, S_i is the measured signal on image i, E_e is the encircled energy in the aperture, S_{Tel} is the telescope collecting surface, T_r is the transmission of the atmosphere, telescope and instrument and t_i is the exposure time for image i (100 s in our case).

We consider that we are in a case where we know the value of the encircled energy E_e in the aperture. This value varies mostly with seeing conditions because the AO correction will concentrate more energy in the PSF core when seeing improves. Moreover, we consider that the planet position is known exactly to centre the aperture on the planet PSF and avoid photometric error bias induced by inaccurate centring. Finally, we also take into account the error induced by the field rotation. When the field rotates, it will slowly smear the planet PSF, especially at large angular separations. The effect in our case is significant at separations larger than 1.0 arcsec because we simulated long exposures for individual images (100 s). In practice, exposures for individual images will typically last a few seconds to avoid detector saturation, reducing the effect of PSF smearing up to a few arcsec.

4.3 Photometric accuracy in ADI

For our simulated test case, the planet flux has been evaluated in all data cubes after using the ADI data analysis method. In each filter pair and for each simulated planet, two independent values are obtained at λ_0 and λ_1. They are compared to the flux value introduced at the beginning of the simulation to evaluate the photometric error. Fig. 2 (left) illustrates the photometric performance as a function of wavelength and angular separation. The contours indicate the contrast value between the star and planet below which the photometric precision is better than 0.2 mag. Such a precision is necessary in order to be able to disentangle between different planet masses when comparing actual measurements to evolutionary models. We see two major effects: (i) the photometric performance clearly depends on wavelength; (ii) there are two different regimes depending on the position compared to the AO control radius. The first effect is directly related to the chromaticity of the PSF. In the speckle-limited regime, the noise attenuation is almost constant with angular separation compared to the coronagraphic profile, and the level of the coronagraphic profile linearly depends on wavelength. The second effect is related to the AO correction inside the control radius. Inside this region, we see a stabilization of the performance: 0.2 mag photometric precision can be reached up to contrast of 10–11 mag (10^{-4} to 4×10^{-4}) from 0.2 arcsec to the AO control radius, which extends from 0.5 arcsec in the Y band to 1.0 arcsec in the K band. Outside the AO control radius, the photometric performance increases almost linearly with angular separation at all wavelengths to reach contrast values of 14–15 mag (2.5×10^{-6} to 10^{-6}) around 2.0 arcsec. These numbers are given in the context of our simulated test case, but the general effects should be similar for any data obtained with high-contrast coronagraphic imagers.

4.4 Photometric accuracy in SDI+ADI

Similarly to the noise level, using the SDI+ADI data analysis method improves the photometric accuracy. However, using SDI+ADI will only provide an estimation of the differential flux of the planet between the two filters, in contrast to ADI, which provides an absolute measurement. To preserve the planet differential flux, the amplitude correction factor, usually applied for SDI in the subtraction, is taken equal to a fixed value of 1. The photometric

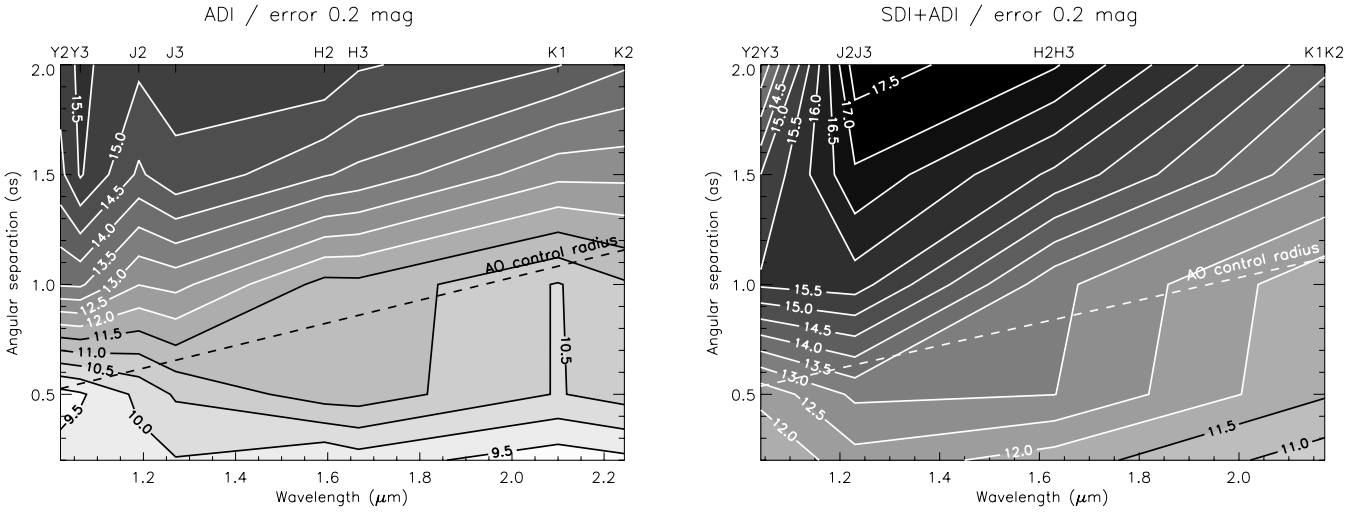

Figure 2. Magnitude difference between the star and the planet for which the photometric precision is better than 0.2 mag, as a function of wavelength and angular separation using ADI (left) and SDI+ADI (right) data analysis methods. The oblique dashed line shows the AO control radius limit.

error estimated with SDI+ADI follows the same variations as for ADI, but at higher contrast values. Fig. 2 (right) illustrates the photometric performance as a function of wavelength and angular separation in SDI+ADI. The trends are similar to ADI alone, but the chromatic effect is less significant because the PSF chromaticity has been mitigated by the SDI part of the analysis. Compared to ADI alone, the contrast values at which a 0.2-mag photometric error is reached are 1.5–2.5 mag higher. At shorter wavelengths, in Y2Y3 filters, performances at separations larger than 1.0 arcsec decrease. This effect is related to the size of the aperture for photometry that is very small in the *Y* band (four pixels in diameter), and to the field rotation which has a strong effect on encircled energy at separations larger than 1.0 arcsec in the *Y* band. Considering shorter exposures for individual images where the field rotation is negligible would decrease the photometric errors in this particular case.

4.5 Empirical photometric accuracy

We hereafter combine the photometric accuracy obtained in ADI and SDI+ADI to define empirical photometric error curves for each filter pair as a function of contrast. The photometric error curves as a function of contrast at each angular separation have been fitted with the empirically defined function:

$$phot_{\rm err} = \frac{p_1}{c^{p_2}} + p_3 \qquad (2)$$

where $phot_{\rm err}$ is the photometric error, c is the contrast and (p_1, p_2, p_3) are the fitted parameters. This function approaches the measured points with a precision of $\sim$1 per cent. The fitting has been performed for ADI and SDI+ADI. To take into account the scattering of the error with the planet's position in the images, different cases have been considered at each separation, corresponding to the three different simulated planet positions: a standard case with an average photometric error, an optimal case corresponding to the lowest estimation of the error and a pessimistic case corresponding to the upper estimation of the error. These empirical photometric errors are plotted in Fig. 3 for the four simulated filter pairs. The amplitude of the error bars is defined by the optimal and pessimistic error curves described above. We assume that the photometric error in ADI is the same in the two filters of a pair, which is legitimate given the amplitude of the error bars. These empirical error curves lie in the same range as the expected photometric accuracy of other data analysis methods developed within the SPHERE consortium by Mugnier et al. (2008) and Smith et al. (2009).

Table 3 gives for each filter pair and each angular separation the contrast value at which the photometric error in ADI becomes lower than the differential photometric error in SDI+ADI. These values give the contrast at which it becomes more interesting in terms of photometric error to obtain a differential flux estimation. As explained in Section 4.4, aperture photometry in the *Y* band is extremely sensitive to errors introduced by the position of the

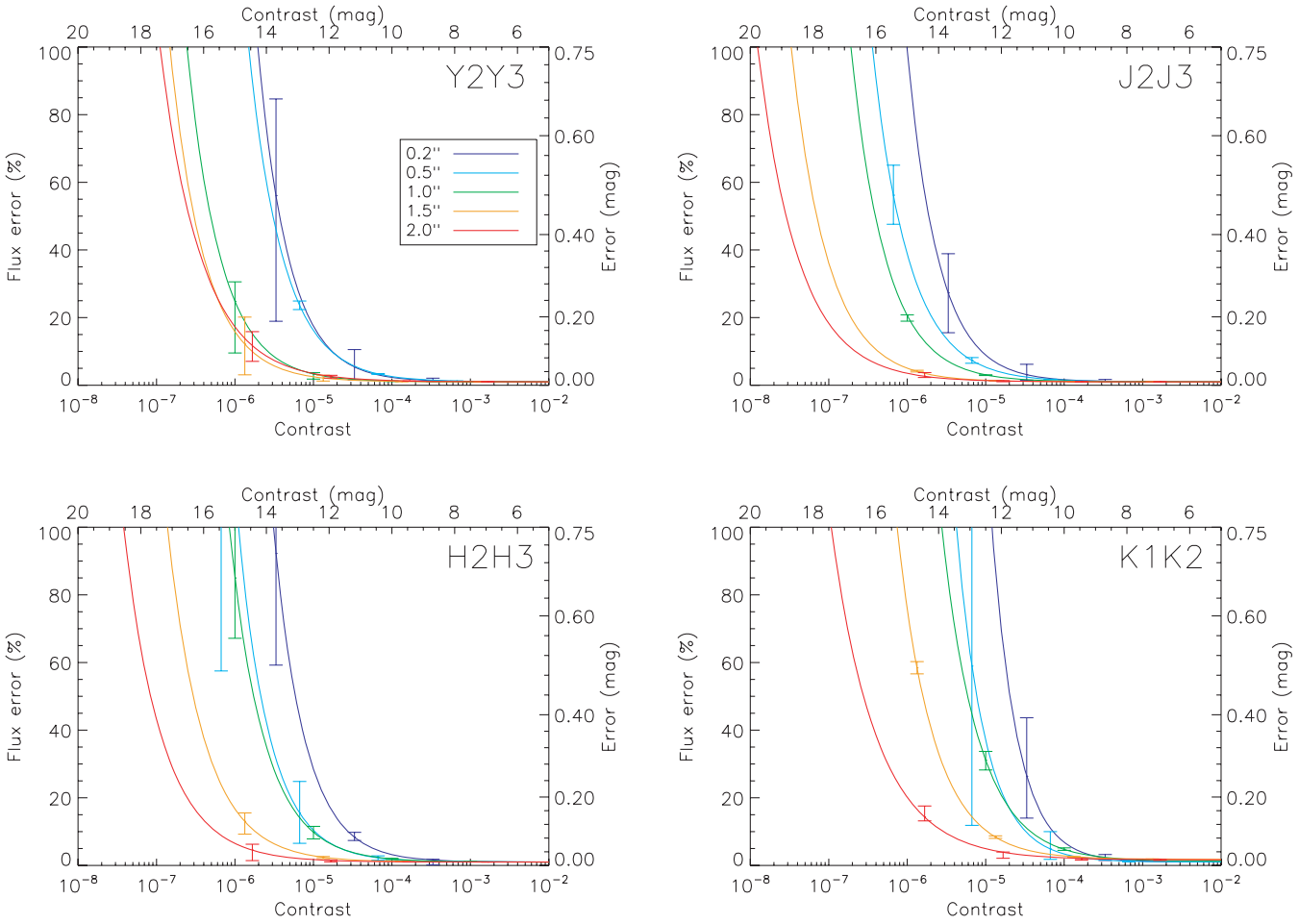

Figure 3. Empirical photometric error as a function of contrast in IRDIS filter pairs using either ADI or SDI+ADI data analysis methods. Errors bars have been represented only for a small set of data points. Their amplitude is defined by the optimal and pessimistic error curves described in the text.

Table 3. Contrast limit over which the differential photometric error in SDI+ADI becomes smaller than the photometric error in ADI.

	Filter pair			
Separation (arcsec)	Y2Y3 (mag)	J2J3 (mag)	H2H3 (mag)	K1K2 (mag)
0.2	6.8	6.8	6.5	6.8
0.5	6.0	6.8	8.3	8.0
1.0	10.8	9.3	8.0	7.2
1.5	12.8	11.0	11.0	10.0
2.0		11.5	12.2	12.2

aperture or the field rotation because the aperture is very small. This is why in the Y2Y3 pair at 2.0 arcsec there is no contrast limit between ADI and SDI+ADI; for this particular case, the flux estimation error is slightly better in ADI than SDI+ADI.

5 PHOTOMETRIC CHARACTERIZATION

In this section we evaluate the characterization capabilities of IRDIS in imaging mode (i.e. how well the physical parameters $T_{\rm eff}$ and $\log g$ of the planets can be estimated from photometric measurements in different spectral bands).

5.1 Characterization simulation

To estimate the characterization capabilities of IRDIS, we performed a new simulation, using as input the 5σ detection limits obtained from Section 4.1 and the empirical error curves obtained in Section 4.5. The goal of the simulation was to test the efficiency of all filter pair sequences for characterization at different stellar magnitudes and for a large number of planetary atmosphere models. These simulations are based on current state-of-the-art atmosphere models. Although these models will clearly evolve with new detections in the future, they allow us to test the expected performances of IRDIS, as well as to estimate the intrinsic errors of our signal extraction and comparison to models. It has been performed for all stellar types and atmosphere models included in our library (see Table 2).

For the simulation we assume that the same planetary system is observed with different filter pairs in a given order. For each possible combination of parameters (filter pair sequence, star magnitude, angular separation, planet atmosphere model) we proceed as follows. The star and planet fluxes are calculated in the filters of the first pair. If the planet is not detectable (considering the 5σ detection limit), the simulation for that combination of parameters is stopped. If it is indeed detectable, a photometric measurement is obtained. Depending on the contrast between the planet and the star in each filter, different information is obtained: two direct photometric measurements if the planet is detectable with ADI in both filters, a differential flux measurement if the planet is only detectable with SDI+ADI or a direct and a differential measurement if the planet is only detectable in ADI in one of the filters. Once the flux measurements are obtained, the photometric error is determined from the empirical error curves and added to the measured values to obtain lower and upper limits to the planet flux. Models that can correspond to these limits are then searched for in our library of models. If only one model corresponds, we stop iterations, considering that the planet has been fully characterized within the limits of the grid of atmosphere models that is used. If many models match these limits, we switch to the next filter pair in the sequence, and the same process is started again. In a given sequence, each filter will bring some additional information that will help to find the appropriate atmosphere model and constrain the values of $T_{\rm eff}$ and $\log g$. At the end of the filter pair sequence, four distinct outcomes are possible, as follows.

(i) Non-detection (ND): the planet is not detected in the first filter pair; the sequence is stopped.

(ii) Non-unique characterization (NC): the planet is detected at least in the first filter pair of the sequence; at the end of the sequence, many models match the flux measurements and they have different values of $T_{\rm eff}$ and $\log g$.

(iii) $T_{\rm eff}$ characterization (TC): the planet is detected at least in the first filter pair of the sequence; at the end of the sequence, many models match the flux measurements and they all share the same value for $T_{\rm eff}$ but not for $\log g$.

(iv) Full characterization (FC): the planet is detected at least in the first filter pair of the sequence; at the end of the sequence, only one model matches the flux measurements, which means that the $T_{\rm eff}$ and $\log g$ values have been determined.

TC and FC are considered within the limits of the grid of atmosphere models, which is 100 K in $T_{\rm eff}$ and 0.5 in $\log g$ (i.e. the full characterization corresponds to the determination of $T_{\rm eff}$ and $\log g$ with an error equal to the limits of the model grid). Another important point is that, in practice, the photometric error will have to be estimated from the science data. Although we consider here an ideal case where the photometric error is known, other data analysis methods, such as that proposed by Smith et al. (2009), will allow direct estimation of the error from the data, with a precision that is compatible with the results presented here.

5.2 Filter pair sequence analysis

The output of this simulation allows us to determine the most significant filter pair sequence for characterization (i.e. the sequence that maximizes the number of characterizations). The strategy is to progressively build an optimal sequence by adding each time the filter pair that increases the most the number of characterizations. All possible filter pair sequences have been systematically tested to find the one that maximizes the number of $T_{\rm eff}$ characterizations and full characterizations (TC+FC), as a function of stellar magnitude. The simulation shows the following important results (see Table 4 for details).

(i) H2H3 is the filter pair that minimizes the number of non-detections, reflecting the fact that the CH_4 absorption band near 1.6 μm in the spectra of cool substellar objects is the optimal feature for their detection. However, it should be noted that this specific spectral feature might not always be present in lower-mass objects, as mentioned in Section 2.

(ii) When adding a new filter pair to a sequence, adding Y2Y3 or J2J3 will increase the number of characterized models more than H3H4 or K1K2. This result does not depend on the stellar magnitude.

(iii) The scattering of the flux error between the pessimistic optimal photometric error curves has no major influence on the number of characterized models when more than one filter pair is used. In particular, we see the error bars of the different flux cases do not significantly overlap, confirming that the chosen sequence is appropriate for all cases of flux.

Table 4. Analysis of the filter pair sequences.

Spectral type	P1[a]	P2[a]	P3[a]	P4[a]	P5[a]	ND[b] (per cent)	NC[c] (per cent)	TC[d] (per cent)	FC[e] (per cent)	TC+FC (per cent)
M0	H2H3					3	20^{+1}_{-1}	0	77^{+1}_{-1}	77^{+1}_{-1}
$V = 8.8$	H2H3	Y2Y3				3	2^{+1}_{-1}	0	95^{+1}_{-1}	95^{+1}_{-1}
$H = 5.3$	H2H3	Y2Y3	J2J3			3	1^{+0}_{-1}	0	96^{+1}_{-1}	96^{+1}_{-0}
	H2H3	Y2Y3	J2J3	H3H4		3	1^{+0}_{-1}	0	96^{+1}_{-1}	96^{+1}_{-0}
	H2H3	Y2Y3	J2J3	H3H4	K1K2	3	1^{+0}_{-1}	0	96^{+1}_{-1}	96^{+1}_{-0}
K0	H2H3					6	35^{+1}_{-8}	0	59^{+8}_{-1}	59^{+8}_{-1}
$V = 5.9$	H2H3	Y2Y3				6	4^{+2}_{-1}	2^{+1}_{-1}	88^{+3}_{-2}	90^{+2}_{-1}
$H = 4.0$	H2H3	Y2Y3	J2J3			6	2^{+1}_{-1}	1^{+0}_{-1}	92^{+1}_{-1}	92^{+1}_{-1}
	H2H3	Y2Y3	J2J3	H3H4		6	2^{+1}_{-1}	1^{+0}_{-0}	92^{+1}_{-1}	92^{+1}_{-1}
	H2H3	Y2Y3	J2J3	H3H4	K1K2	6	2^{+1}_{-1}	1^{+0}_{-0}	92^{+1}_{-1}	92^{+1}_{-1}
G0	H2H3					7	43^{+3}_{-7}	0	50^{+7}_{-3}	50^{+7}_{-3}
$V = 4.4$	H2H3	Y2Y3				7	7^{+4}_{-2}	3^{+1}_{-1}	83^{+5}_{-3}	86^{+4}_{-2}
$H = 3.0$	H2H3	Y2Y3	J2J3			7	3^{+1}_{-1}	2^{+1}_{-1}	88^{+2}_{-2}	90^{+1}_{-1}
	H2H3	Y2Y3	J2J3	H3H4		7	3^{+1}_{-1}	1^{+1}_{-1}	88^{+2}_{-2}	90^{+1}_{-1}
	H2H3	Y2Y3	J2J3	H3H4	K1K2	7	3^{+1}_{-1}	1^{+1}_{-1}	88^{+2}_{-2}	90^{+1}_{-1}
F0	H2H3					10	55^{+3}_{-7}	0	35^{+7}_{-3}	35^{+7}_{-3}
$V = 2.7$	H2H3	J2J3				10	11^{+2}_{-2}	3^{+0}_{-1}	76^{+2}_{-3}	79^{+2}_{-2}
$H = 1.5$	H2H3	J2J3	Y2Y3			10	7^{+3}_{-3}	3^{+1}_{-1}	80^{+4}_{-4}	83^{+3}_{-3}
	H2H3	J2J3	Y2Y3	H3H4		10	6^{+2}_{-2}	2^{+1}_{-1}	82^{+4}_{-3}	84^{+2}_{-2}
	H2H3	J2J3	Y2Y3	H3H4	K1K2	10	6^{+2}_{-2}	2^{+1}_{-1}	82^{+4}_{-3}	84^{+2}_{-2}

[a]P1–P5 designate the filter pairs. [b]Not detected. [c]No characterization. [d]$T_{\rm eff}$ characterization. [e]Full characterization.

This last result is particularly important as it advocates for a given sequence of filter pairs and allows us to set general priorities on the filter pairs for characterization. When there are no a priori assumptions on the nature of the objects, the priorities are defined from highest to lowest as follows:

0. H2H3;
1. Y2Y3/J2J3;
2. H3H4/K1K2.

H2H3–Y2Y3–J2J3–H3H4–K1K2 is referred to as the optimal sequence from now on, and we only consider the standard empirical errors, as the differences with the other error curves are small. Assuming the use of the optimal sequence, Fig. 4 represents the proportion of characterized models (TC+FC) from our library when new filter pairs are added. The trends are identical for the four different stellar magnitudes. When using only H2H3, the proportion of characterized models is comprised between 30 and 80 per cent, and the error bars are of ∼10 per cent for bright stars. Adding a second filter pair greatly improves the proportion of characterized models, which is above 70 per cent for all stellar magnitudes. Adding more filter pairs confirms this trend and tends to reduce the error bars to less than 5 per cent for all magnitudes. The main conclusion is that most of the information for characterizing any given model is obtained using two filter pairs around low-mass stars when the contrast is favourable, and three filter pairs around high-mass stars, for which the contrast is more challenging.

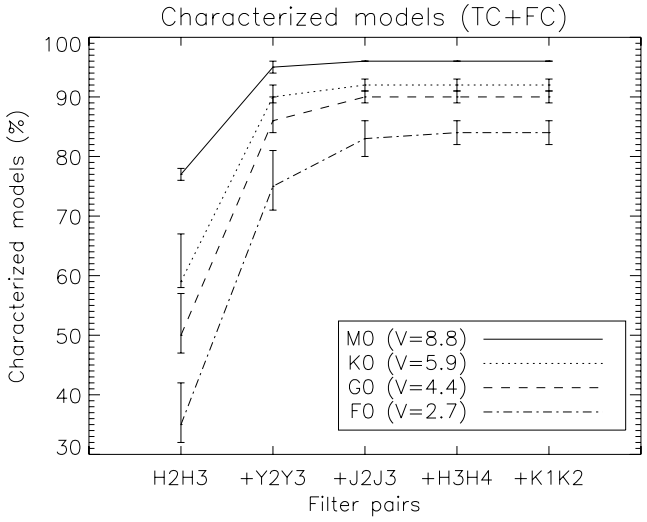

Figure 4. Proportion of models in our library characterized by adding filter pairs from the optimal filter pair sequence for four stellar magnitudes. The error bars are given by the optimal and pessimistic photometric error curves.

5.3 Lowest estimations of $T_{\rm eff}$

In the previous section, we set priorities for characterization on the different filter pairs of IRDIS. We now detail the lowest values of $T_{\rm eff}$ that IRDIS will be able to characterize as a function of stellar magnitude and angular separation. Fig. 5 gives the smallest values of $T_{\rm eff}$, which have been characterized when using one to three filter pairs from the optimal sequence. Colder planets can be detected, but we were not able to find the appropriate values of $T_{\rm eff}$ and $\log g$. When using only H2H3, planets with $T_{\rm eff}$ down to 900 K should be characterized at an angular separation of 0.2 arcsec from high-mass bright stars and 700 K from lower-mass stars. Adding a second filter

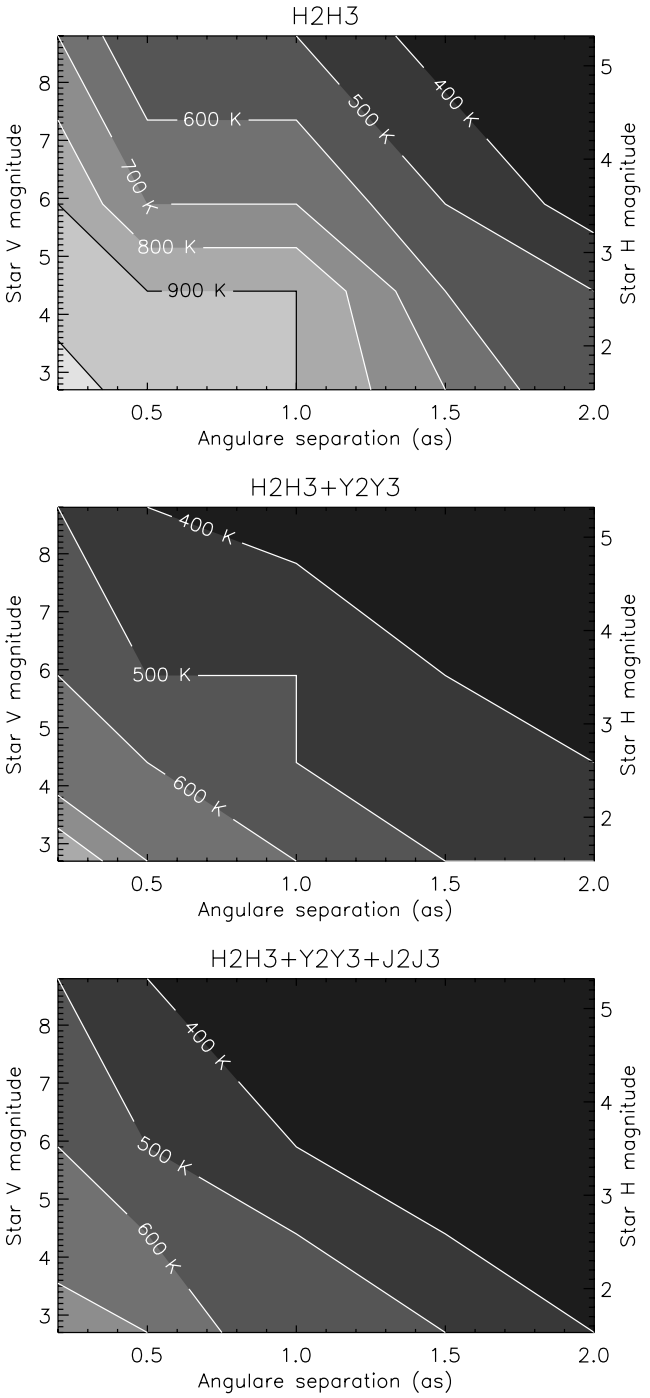

Figure 5. Smallest value of $T_{\rm eff}$ that can be characterized as a function of star magnitude (*y*-axis) and angular separation (*x*-axis) when using one, two or three filters from the optimal sequence.

pair considerably improves these results by 200 K, while adding a third pair confirms these limiting values.

With the considered data analysis methods, and according to the evolutionary models from Baraffe et al. (2003) for the COND atmosphere models, we can estimate that in a very young system of 10 Myr, we should be able to characterize a planet of 1 $M_{\rm Jup}$ with H2H3 at separations larger than 0.5 arcsec around a low-mass star (M0 at 10 pc) where the star–planet contrast is favourable, but only further than 2.0 arcsec around a high-mass star (F0 at 10 pc) where the contrast difference is larger. With two filter pairs, the limit would be 0.2 arcsec around a low-mass star and 1.0 arcsec around a high-mass star. For older systems, only planets of a few Jupiter masses could be characterized. At 100 Myr, a Jupiter-mass planet would remain out of reach for characterization with H2H3 filters around a high-mass star, and only at separations larger than 1.5 arcsec around a low-mass star. At this age, the $T_{\rm eff}$ limits of 700 and 500 K, which can be reached at small angular separation around high- and low-mass stars, would respectively correspond to planets with masses of $\sim$6.5 $M_{\rm Jup}$ and $\sim$3 $M_{\rm Jup}$. Using improved signal extraction methods, providing more accurate photometry of the companion would certainly push down these limits.

5.4 Study of the non-unique characterizations

NCs are the cases where several models correspond to the flux measurements in all filter pairs with which they are detected. From these remaining models, it is possible to determine if a combination of ($T_{\rm eff}$; $\log g$) is more represented than others, making this combination the most probable values of $T_{\rm eff}$ and $\log g$. If several combinations are counted an equal number of times, an average value and an error can be determined for the values of $T_{\rm eff}$ and $\log g$. In any case, the error is at least equal to the steps in the grids of models. The estimation of the most probable values for $T_{\rm eff}$ and $\log g$ has been performed for all non-uniquely characterized models at all simulated angular separations and magnitudes.

Fig. 6 shows a histogram of the errors on $T_{\rm eff}$ and $\log g$ when using the H2H3 filter pair for high-mass (F0 at 10 pc) and low-mass (M0 at 10 pc) stars. NCs are mostly dominated by errors on the determination of $\log g$. In particular, we see that around a low-mass star, where the contrast is more favourable, the proportion of models with no error on $T_{\rm eff}$ increases by $\sim$20 per cent, while the errors on $\log g$ keep the same distribution. Adding other filter pairs improves the determination of $T_{\rm eff}$ for the non-unique characterizations, in particular around high-mass (brighter) stars, reaching more than 95 per cent for all stellar magnitudes. The determination of $\log g$ is also improved, but even when using three filter pairs the number of cases where the error is less or equal to 0.5 never reaches more than 85 per cent around a high-mass star or 95 per cent around a low-mass star.

5.5 Impact of errors on $T_{\rm eff}$ and $\log g$

The influence of errors on the determination of $T_{\rm eff}$ and $\log g$ on the determination of the planet's mass can be studied using evolutionary models, such as those published by Baraffe et al. (2003) for the COND atmosphere models. The preliminary version of the SPHERE target list (S. Desidera, private communication) was used to define a standard young test case based on age considerations. The average age for targets younger than 100 Myr is 44 $\pm$ 20 Myr and the average error on the determination of the target age is 30 Myr. Using these values, we can define two test cases considering a planet of 2 $M_{\rm Jup}$ aged 44 $\pm$ 30 Myr orbiting at 5 au from M0 and F0 stars at 10 pc. According to the evolutionary models from Baraffe et al. (2003), such planets should have $T_{\rm eff}$ = 516 K and $\log g$ = 3.54 dex, resulting in a contrast of 11.9 and 15.6 mag in the *H* band, around the M0 and F0 stars, respectively. Considering the results from Sections 5.3 and 5.4, the planet around the F0 star cannot be characterized with IRDIS using one filter pair, while the planet around the M0 star is close to the measured limit.

The expected spectra of these planets were introduced in our simulation to test the accuracy of extracting flux information and

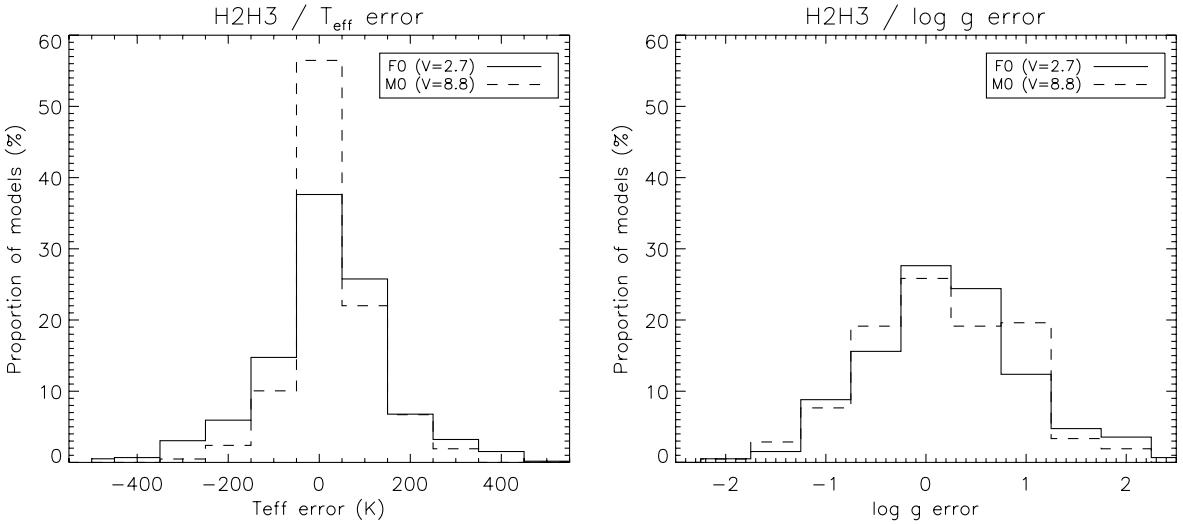

Figure 6. Distribution of the errors on $T_{\rm eff}$ and $\log g$ for non-unique characterizations with the H2H3 filter pair around a high-mass star (F0 at 10 pc, solid line) and a low-mass star (M0 at 10 pc, dashed line).

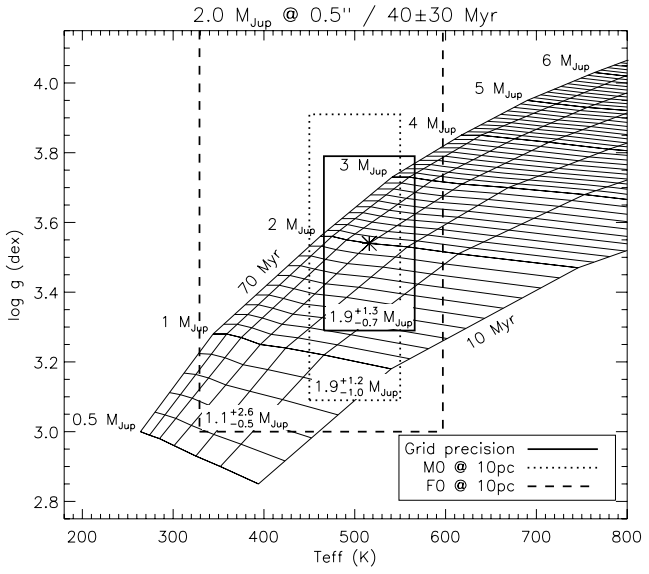

Figure 7. Isochrones for the COND planetary atmosphere models covering an age of 40 ± 30 Myr used for the determination of the mass of hypothetical 2-$M_{\rm Jup}$ planets orbiting at 5 au from M0 and F0 stars at 10 pc. The error boxes defined by the possible values for $T_{\rm eff}$ and $\log g$ of both planets are represented by dotted and dashed rectangles, respectively. The planet mass derived from the models and error box is displayed at the bottom-left corner of each error box (see text for an explanation on how the planet masses are derived). The position of the planet predicted by the evolutionary models is represented by the star symbol, and the error box defined by the atmosphere model grid precision is given for reference around that position by a plain rectangle.

inversely deriving physical parameters, and to estimate their mass using evolutionary models. The results are presented in Fig. 7. The areas covered by the values of $T_{\rm eff}$ and $\log g$ are shown as rectangular boxes on the predicted isochrones for both planetary systems. The bin size of the atmosphere model grid is also plotted for reference. For each case, the planet mass is estimated by selecting all the isochrones of the masses that cross the error box and weighting them by the integral of the isochrone inside the box. The isochrone that has the largest intersection with the error box is supposed to be the most likely (or the average if several isochrones have the same integral). The upper and lower limits of the mass are given by the highest and lowest mass isochrones that cross the box.

Around a low-mass star, the parameters $T_{\rm eff}$ and $\log g$ are estimated with an accuracy close to that given by the atmosphere model grid ($1.9^{+1.3}_{-0.7}$ $M_{\rm Jup}$), leading to an estimation of $1.9^{+1.2}_{-1.0}$ $M_{\rm Jup}$. Around a high-mass star, the planet is very close to the detection limit at 0.5 arcsec, resulting in a poor estimation of both $T_{\rm eff}$ and $\log g$. The important photometric error in H2H3 leads to a very large uncertainty on $\log g$ (4.33 ± 1.23). The mass of the planet is then estimated to $1.1^{+2.6}_{-0.5}$ $M_{\rm Jup}$. In this case, the planet mass is greatly underestimated, and the large uncertainties on $T_{\rm eff}$ and $\log g$ lead to a large upper limit for the mass estimation. The origin of the large offset on the determination of $\log g$ is still uncertain, and further simulations are still needed to investigate thoroughly the complete parameter space. In particular, we see in this case that the age uncertainty unquestionably increases the uncertainty on the mass estimation, by increasing the number of isochrones crossing the possible values of $T_{\rm eff}$ and $\log g$. Such simulations would greatly benefit from updated homogeneous atmosphere model grids covering a large span of $T_{\rm eff}$, $\log g$ and age.

6 CONCLUSIONS

Next-generation instruments, such as SPHERE and GPI, for ground-based direct imaging of exoplanets will provide data intrinsically limited by speckle noise. This noise needs to be attenuated using a posteriori data analysis methods, such as SDI and ADI. In this paper, we have quantified the exoplanet characterization capabilities of IRDIS, the differential imager of SPHERE, using photometric and differential photometric information.

The photometric performances have been evaluated using aperture photometry on the detectable planets as a function of contrast and wavelength for a standard test case. In particular, we have shown that the photometric performance depends very much on wavelength, because of the PSF chromaticity, and on the position with respect to the AO control radius. With ADI, a photometric accuracy of 0.2 mag is reached inside the AO control radius for contrast values of 10–11 mag between the star and planet, while at larger radii this precision can be reached for contrasts up to 15 mag.

With SDI+ADI, the overall photometric performance is improved, increasing by 1.5–2.5 mag the contrast at which a 0.2-mag precision is reached.

We have defined the empirical photometric accuracies for IRDIS in its different filter pairs; these were used to test the characterization capabilities of IRDIS with all possible combinations of filter pairs. The priorities for characterization have been set on the different filter pairs by finding the pairs that maximize the number of possible characterizations in various conditions. We have shown that when there is no a priori knowledge of the planet, the filter pairs Y2Y3 and J2J3 allow a larger number of characterizations than the pairs H3H4 and K1K2. Then, we have shown that by using filter pair H2H3, it will be possible to characterize planets with $T_{\rm eff} \simeq 900$ K around high-mass stars at small angular separation, and $T_{\rm eff} \simeq 700$ K around lower-mass stars. Adding Y2Y3 and J2J3 filter pairs allows us to decrease the characterizable $T_{\rm eff}$ by 200 K at all separations and for all stellar magnitudes, while considerably decreasing the number of non-characterizations for warmer planets.

Finally, we have shown that non-unique characterizations (i.e. planets for which the $T_{\rm eff}$ and $\log g$ values could not be determined exactly, within the limits of the grid of atmosphere models) are mostly dominated by errors on the determination of $\log g$. In particular, we have shown that around low-mass stars, where the contrast is more favourable, the determination of $T_{\rm eff}$ is largely improved, while the errors on $\log g$ remain identical around a high-mass star. Considering evolutionary models, and including typical ages from the future SPHERE target list, we have shown that such errors on the determination of a low-mass planet (2 $M_{\rm Jup}$) results in a large uncertainty around a high-mass bright star, but is very close to the limits fixed by the model grid around a fainter low-mass star.

In this paper, we have shown that IRDIS, the dual-band imager of SPHERE, should be able to fulfil the goal set for a high-contrast imager (i.e. the ability to detect and characterize planetary companions down to the Jupiter mass around nearby young stars). Similar developments could also be achieved for an IFS in the future, allowing us to quantify precisely the performances of SPHERE in the near-infrared, and to work on the aspect of characterization strategy for the detected objects.

ACKNOWLEDGMENTS

We wish to thank Silvano Desidera (INAF) for generously providing a preliminary version of the SPHERE target list with all associated physical parameters, and Laurent Mugnier (ONERA) for providing an optimized procedure for spatial rescaling of the images.

SPHERE is an instrument designed and built by a consortium consisting of Laboratoire d'Astrophysique de Grenoble (LAOG), Max-Planck-Institut für Astronomie (MPIA), Laboratoire d'Astrophysique de Marseille (LAM), Laboratoire d'études spatiales et d'instrumentation en astrophysique (LESIA), Laboratoire Fizeau, Istituto Nazionale di Astrofisica (INAF), Observatoire de Genève, Swiss Federal Institute of Technology (ETH), Netherlands Research School for Astronomy (NOVA), Office National d'Etudes et Recherches Aérospatiales (ONERA) and Netherlands Institute for Radio Astronomy (ASTRON) in collaboration with the ESO.

REFERENCES

Ackerman A. S., Marley M. S., 2001, ApJ, 556, 872
Aime C., Soummer R., 2004, ApJ, 612, L85
Allard F., Hauschildt P. H., Alexander D. R., Tamanai A., Schweitzer A., 2001, ApJ, 556, 357
Allard F., Guillot T., Ludwig H.-G., Hauschildt P. H., Schweitzer A., Alexander D. R., Ferguson J. W., 2003, in Martín E., ed., Proc. IAU Symp. 211, Model Atmospheres and Spectra: The Role of Dust. Kluwer, Dordrecht, p. 325
Allard F., Allard N. F., Homeier D., Kielkopf J., McCaughrean M. J., Spiegelman F., 2007, A&A, 474, L21
Aller-Carpentier E. et al., 2008, Proc. SPIE, 7015, 108
Angel J. R. P., 1994, Nat, 368, 203
Baraffe I., Chabrier G., Barman T. S., Allard F., Hauschildt P. H., 2003, A&A, 402, 701
Beuzit J.-L. et al., 2006, The Messenger, 125, 29
Burrows A. et al., 1997, ApJ, 491, 856
Burrows A., Sudarsky D., Hubeny I., 2006, ApJ, 640, 1063
Carbillet M. et al., 2004, Proc. SPIE, 5490, 637
Carbillet M. et al., 2008, Proc. SPIE, 7015, 191
Castelli F., Kurucz R. L., 2003, in Piskunov N., Weiss W. W., Gray D. F., eds, Proc. IAU Symp. 210, New Grids of ATLAS9 Model Atmospheres. Kluwer, Dordrecht, p. 20
Chabrier G., Baraffe I., Allard F., Hauschildt P., 2000, ApJ, 542, 464
Chauvin G., Lagrange A.-M., Dumas C., Zuckerman B., Mouillet D., Song I., Beuzit J.-L., Lowrance P., 2005a, A&A, 438, L25
Chauvin G. et al., 2005b, A&A, 438, L29
Dohlen K. et al., 2008a, Proc. SPIE, 7014, 118
Dohlen K., Saisse M., Origne A., Moreaux G., Fabron C., Zamkotsian F., Lanzoni P., Lemarquis F., 2008b, Proc. SPIE, 7018, 170
Fitzgerald M. P., Graham J. R., 2006, ApJ, 637, 541
Fortney J. J., Marley M. S., Hubickyj O., Bodenheimer P., Lissauer J. J., 2005, Astron. Nach., 326, 925
Fortney J. J., Marley M. S., Saumon D., Lodders K., 2008, ApJ, 683, 1104
Fusco T. et al., 2006, Proc. SPIE, 6272, 17
Goodman J. W., 1968, Introduction to Fourier Optics. McGraw-Hill, New York
Hinkley S. et al., 2007, ApJ, 654, 633
Hodapp K. W. et al., 2008, Proc. SPIE, 7014, 42
Itoh Y. et al., 2005, ApJ, 620, 984
Janson M., Bergfors C., Goto M., Brandner W., Lafrenière D., 2010, ApJ, 710, L35
Kalas P. et al., 2008, Sci, 322, 1345
Kurucz R. L., 1979, ApJS, 40, 1
Lafrenière D., Marois C., Doyon R., Nadeau D., Artigau É., 2007, ApJ, 660, 770
Lafrenière D., Jayawardhana R., van Kerkwijk M. H., 2008, ApJ, 689, L153
Lagrange A. M. et al., 2009, A&A, 493, L21
Langlois M., 2001, PhD thesis, Université de Paris VII (Denis Diderot)
Langlois M., Sandler D. G., Ryan P. T., McCarthy D. W., 1998, Proc. SPIE, 3353, 189
Lenzen R., Close L., Brandner W., Biller B., Hartung M., 2004, Proc. SPIE, 5492, 970
Luhman K. L. et al., 2006, ApJ, 649, 894
Macintosh B., Poyneer L., Sivaramakrishnan A., Marois C., 2005, Proc. SPIE, 5903, 170
Macintosh B. et al., 2006, Proc. SPIE, 6272, 18
Marois C., Doyon R., Racine R., Nadeau D., 2000, PASP, 112, 91
Marois C., Doyon R., Nadeau D., Racine R., Riopel M., Vallée P., Lafrenière D., 2005, PASP, 117, 745
Marois C., Lafrenière D., Doyon R., Macintosh B., Nadeau D., 2006, ApJ, 641, 556
Marois C., Lafrenière D., Macintosh B., Doyon R., 2008a, ApJ, 673, 647
Marois C., Macintosh B., Barman T., Zuckerman B., Song I., Patience J., Lafreniere D., Doyon R., 2008b, Sci, 322, 1348
Mawet D., Riaud P., Baudrand J., Baudoz P., Boccaletti A., Dupuis O., Rouan D., 2006, A&A, 448, 801
Metchev S., Marois C., Zuckerman B., 2009, ApJ, 705, L204
Mohanty S., Jayawardhana R., Huélamo N., Mamajek E., 2007, ApJ, 657, 1064
Mugnier L. M., Cornia A., Sauvage J.-F., Védrenne N., Fusco T., Rousset G., 2008, Proc. SPIE, 7015, 60

Neuhäuser R., Guenther E. W., Wuchterl G., Mugrauer M., Bedalov A., Hauschildt P. H., 2005, A&A, 435, L13
Patience J., King R. R., De Rosa R. J., Marois C., 2010, A&A, in press (arXiv:1003.4507)
Racine R., Walker G. A. H., Nadeau D., Doyon R., Marois C., 1999, PASP, 111, 587
Rouan D., Riaud P., Boccaletti A., Clénet Y., Labeyrie A., 2000, PASP, 112, 1479
Santos N. C., 2008, New Astron. Rev., 52, 154
Smith I., Ferrari A., Carbillet M., 2009, IEEE Trans. Signal Process., 57, 904
Soummer R., 2005, ApJ, 618, L161
Soummer R., Ferrari A., Aime C., Jolissaint L., 2007, ApJ, 669, 642
Sparks W. B., Ford H. C., 2002, ApJ, 578, 543
Stahl S. M., Sandler D. G., 1995, ApJ, 454, L153
Tsuji T., 2005, ApJ, 621, 1033
Vigan A., Langlois M., Moutou C., Dohlen K., 2008, A&A, 489, 1345
Wittenmyer R. A., Endl M., Cochran W. D., 2007, ApJ, 654, 625

This paper has been typeset from a TEX/LATEX file prepared by the author.